

CaSSIS Geometric Calibration: Technical Report

Stepan Tulyakov

Lausanne, Switzerland

Abstract

This report describes geometrical model of CaSSIS camera of ExoMars Trace Gas Orbiter and presents on-ground as well as in-flight calibration methods and procedures that were used to estimate parameters of this model.

Keywords: CaSSIS, geometric camera model, rational distortion model, on-ground calibration, in-flight calibration, star-field calibration

1. Geometric Camera Model

Main goal of geometric camera modeling is to find mathematical model that describes transformation from 3D object space to 2D image space. The geometric camera model consists of following components:

1. Extrinsic model [1, p155-156].
2. Intrinsic model¹ [1, p153-158];
3. Lens distortion model [1, p189-193][2][3][4];

In following sub-sections of this chapter we will describe every component of the model in details.

1.1. Extrinsic Model

Extrinsic model describes coordinate transformation from the spacecraft reference frame to the camera frame (see Figure 1). Having this model and coordinate of the 3D point in the spacecraft reference frame $\mathbf{X}_{\text{ref}} = (X_{\text{ref}}, Y_{\text{ref}}, Z_{\text{ref}})$, we can compute point's coordinate in the camera frame $\mathbf{X} = (X, Y, Z)$ as following

$$\mathbf{X} = \mathbf{R}(\mathbf{X}_{\text{ref}} + \mathbf{t}), \quad (1)$$

¹Intrinsic model is also known as central projection or pinhole model.

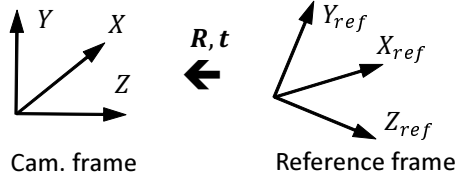


Figure 1: Extrinsic model: spacecraft reference frame \rightarrow camera frame.

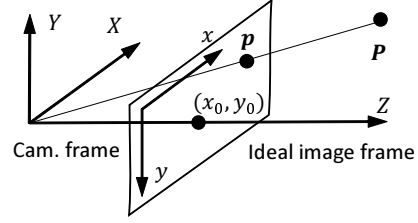


Figure 2: Intrinsic model: camera frame \rightarrow ideal image frame.

were \mathbf{R} is a 3×3 rotation matrix and \mathbf{t} is a 3×1 translation vector. The rotation matrix \mathbf{R} is a matrix function of 3 Euler angles $\mathbf{R} = \mathbf{F}(\alpha, \beta, \gamma)$. It can be factorized as following

$$\mathbf{R} = \mathbf{R}_X \cdot \mathbf{R}_Y \cdot \mathbf{R}_Z, \quad (2)$$

where \mathbf{R}_X , \mathbf{R}_Y and \mathbf{R}_Z are 3×3 rotational matrices, that represent rotations around axes X , Y and Z by angles α , β and γ respectively.

$$\mathbf{R}_X = \begin{bmatrix} 1 & 0 & 0 \\ 0 & \cos \alpha & \sin \alpha \\ 0 & -\sin \alpha & \cos \alpha \end{bmatrix}, \quad (3)$$

$$\mathbf{R}_Y = \begin{bmatrix} \cos \beta & 0 & -\sin \beta \\ 0 & 1 & 0 \\ \sin \beta & 0 & \cos \beta \end{bmatrix}, \quad (4)$$

$$\mathbf{R}_Z = \begin{bmatrix} \cos \gamma & \sin \gamma & 0 \\ -\sin \gamma & \cos \gamma & 0 \\ 0 & 0 & 1 \end{bmatrix}, \quad (5)$$

11 The extrinsic camera model has 6 degree-of-freedom (DOF) in total.

12 1.2. Intrinsic Model

Intrinsic model [1, p153-158] describes coordinate transformation from the 3D camera frame (see Figure 2). Having this model and coordinates of the 3D point in the camera frame $\mathbf{X} = \{X, Y, Z\}$, we can compute it's coordinates in the 2D image frame $\mathbf{x} = \{x, y\}$ as following

$$(x, y) = \left(\frac{\mathbf{K}_1^T \mathbf{X}}{\mathbf{K}_3^T \mathbf{X}}, \frac{\mathbf{K}_2^T \mathbf{X}}{\mathbf{K}_3^T \mathbf{X}} \right), \quad (6)$$

where $\mathbf{K}_{1,2,3}^T$ are rows of 3×3 upper triangular camera calibration matrix \mathbf{K} :

$$\mathbf{K} = \begin{bmatrix} \alpha_x & 0 & x_0 \\ 0 & \alpha_y & y_0 \\ 0 & 0 & 1 \end{bmatrix}, \quad (7)$$

where α_x and α_y are vertical and horizontal focal lengths of the camera, measured in pixels, and x_0 , y_0 are coordinates of a principal point in the image frame. The intrinsic camera model has 4 DOF in total.

1.3. Lens Distortion Model

Intrinsic camera model is usually complemented with a lens distortion model, that describes transformation between undistorted (ideal) $\mathbf{x} = (x, y)$ and distorted (actual) image coordinates $\mathbf{i} = (i, j)$. Below, we listed several lens distortion models in the order of increasing complexity.

*Radial model*² [1, p189-193]. It is a simplest model with 5 DOF, that accounts only for symmetric radial distortion:

$$\begin{aligned} i &= x + \delta x_r \\ j &= y + \delta y_r, \end{aligned} \quad (8)$$

where δx_r and δy_r are radial distortion components, that are computed as

$$\begin{aligned} \delta x_r &= (x - x_c)(k_1 r^2 + k_2 r^4 + k_3 r^6) \\ \delta y_r &= (y - y_c)(k_1 r^2 + k_2 r^4 + k_3 r^6), \end{aligned} \quad (9)$$

where $r = \sqrt{(x - x_c)^2 + (y - y_c)^2}$ is a distance from a point to the distortion center (x_c, y_c) .

Brown-Conrady model [2]. It is a more complex model with 7 DOF, that accounts for the symmetric radial and tangential decentering distortion:

$$\begin{aligned} i &= x + \delta x_r + \delta x_t \\ j &= y + \delta y_r + \delta y_t, \end{aligned} \quad (10)$$

where δx_r and δy_r are radial distortion components (Equation 9), δx_t and δy_t are tangential distortion components:

$$\begin{aligned} \delta x_t &= p_1(r^2 + 2(x - x_c)^2) + 2p_2(x - x_c)(y - y_c) \\ \delta y_t &= p_2(r^2 + 2(y - y_c)^2) + 2p_1(x - x_c)(y - y_c) \end{aligned} \quad (11)$$

²The Radial model is equivalent to CAHVOR model [5] that has been widely used in NASA missions.

*Rational model*³ [4]. This is an algebraic (not physical) lens distortion model with 18 DOF, that can describe different complex lens distortion. Lets denote χ as 6×1 vector of "lifted" distorted image coordinates:

$$\chi = [i^2 \quad ij \quad j^2 \quad i \quad j \quad 1]^T \quad (12)$$

In this case, undistorted (ideal) image coordinates are computed as

$$(x, y) = \left(\frac{\mathbf{A}_1^T \chi}{\mathbf{A}_3^T \chi}, \frac{\mathbf{A}_2^T \chi}{\mathbf{A}_3^T \chi} \right), \quad (13)$$

where $\mathbf{A}_{1...3}^T$ are rows of 6×3 rational distortion matrix \mathbf{A} .

Bi-cubic model [3]. This is another algebraic lens distortion model with 20 DOF, that can describe complex lens distortions. Lets denote ψ as 10×1 vector of "lifted" distorted image coordinates:

$$\psi = [i^3 \quad i^2j \quad ij^2 \quad j^3 \quad i^2 \quad ij \quad j^2 \quad i \quad j \quad 1]^T \quad (14)$$

In this case, undistorted (ideal) image coordinates are computed as

$$(x, y) = (\mathbf{B}_1^T \psi, \mathbf{B}_2^T \psi), \quad (15)$$

where $\mathbf{B}_{1,2}^T$ are rows of 10×2 matrix \mathbf{B} .

Lens distortion models, mentioned earlier, can be divided into two classes: direct and inverse models. The direct models describe transformation from the ideal coordinates $\mathbf{x} = (x, y)$ to the distorted coordinates $\mathbf{i} = (i, j)$, whereas the inverse models describe the inverse transformation. However, the algebraic Bi-cubic model and Rational model can be used interchangeably in the direct and in the inverse forms [6].

2. Selection of Lens Distortion Model

Before CaSSIS camera became available to us, we were provided with ray-tracing simulation of the camera optics (Table 1). Using this information, we determined most suitable for CaSSIS lens distortion model. In this chapter in section 1 we explain method and procedure that we used to select the lens distortion model, and in section 2 we show our results.

³The Rational lens distortion model should not be confused with Rational camera model. They have same mathematical form, but in contrast to the Rational lens distortion model, the Rational camera model describes whole camera, including lens distortion, intrinsic and extrinsic parameters.

	Ideal x, [mm]	Real i, [mm]	Error, [pix]	Ideal y, [mm]	Real j, [mm]	Error, [pix]
1	0	0	0	0	0	0
2	0	0	0	-3.3911	-3.3846	-0.65
3	0	0	0	-6.7437	-6.7538	1.01
4	0	0	0	3.4094	3.3846	2.48
5	0	0	0	6.8165	6.7538	6.27
6	-5.1358	-5.1385	0.27	0.0022	0	0.22
7	-5.1207	-5.1385	1.78	-3.3866	-3.3846	-0.2
8	-5.1029	-5.1385	3.56	-6.737	-6.7538	1.68
9	-5.1478	-5.1385	-0.93	3.4093	3.3846	2.47
10	-5.1568	-5.1385	-1.83	6.8142	6.7538	6.04
11	-10.2482	-10.2769	2.87	0.0089	0	0.89
12	-10.2183	-10.2769	5.86	-3.3733	-3.3846	1.13
13	-10.2133	-10.3077	9.44	-6.7171	-6.7538	3.67
14	-10.2722	-10.2769	0.47	3.4094	3.3846	2.48
15	-10.2901	-10.2769	-1.32	6.8075	6.7538	5.37
16	5.1358	5.1385	-0.27	0.0022	0	0.22
17	5.1207	5.1385	-1.78	-3.3866	-3.3846	-0.2
18	5.1029	5.1385	-3.56	-6.737	-6.7538	1.68
19	5.1478	5.1385	0.93	3.4093	3.3846	2.47
20	5.1568	5.1385	1.83	6.8142	6.7538	6.04
21	10.2482	10.2769	-2.87	0.0089	0	0.89
22	10.2183	10.2769	-5.86	-3.3733	-3.3846	1.13
23	10.183	10.2769	-9.39	-6.7173	-6.7538	3.65
24	10.2722	10.2769	-0.47	3.4094	3.3846	2.48
25	10.2901	10.2769	1.32	6.8075	6.7538	5.37

Table 1: CaSSIS ray-tracing lens distortion simulation results.

Model	Params	Fitting method
Radial	5	Levenberg-Marquardt[1, p600] (lsqnonlin in MATLAB)
Brown-Conrandy	7	Levenberg-Marquardt[1, p600] (lsqnonlin in MATLAB)
Rational	18	Homogeneous Linear Least Square. SVD method [1, p592] (svd in MATLAB)
Bi-cubic	20	Linear Least Square, Normal Equations [1, p591] (pinv in MATLAB)

Table 2: Parameters estimation methods for different models.

2.1. Method and Procedure

To find suitable lens distortion model, we fitted several candidate lens distortion models to the provided simulation data and compared mean error of every model. Since number of provided data points was too small to split them into training set and test set, we used leave-one-out cross-validation technique⁴. The error of each model was computed as mean Euclidean distance between the data points and the points predicted by the model in the distorted or the ideal image frames. Model fitting methods, that we used to fit models, are shown in Table 2.

2.2. Results

The model fitting results are shown in Figure 3. Summarizing the results, we can make following conclusions:

1. Basic Radial model fails to represent CaSSIS lens distortion. This is because this model can represent only symmetric distortion, while CaSSIS lens distortion has large asymmetric component.
2. The Brown-Conrandy model performs better, compared to the Radial, but the Bi-cubic and the Rational models are clear winners. They are able to perform distortion correction with 0.1 pixel precision and can be easily fitted to the data using linear least square methods. Among these two models, we prefer the Rational model, since it has less parameters.

⁴It is standard practice in Machine Learning to divide data point into training set, that is used for the model fitting, and test set, that is used for the model evaluation. This helps to detect model over-fitting and make unbiased model comparison.

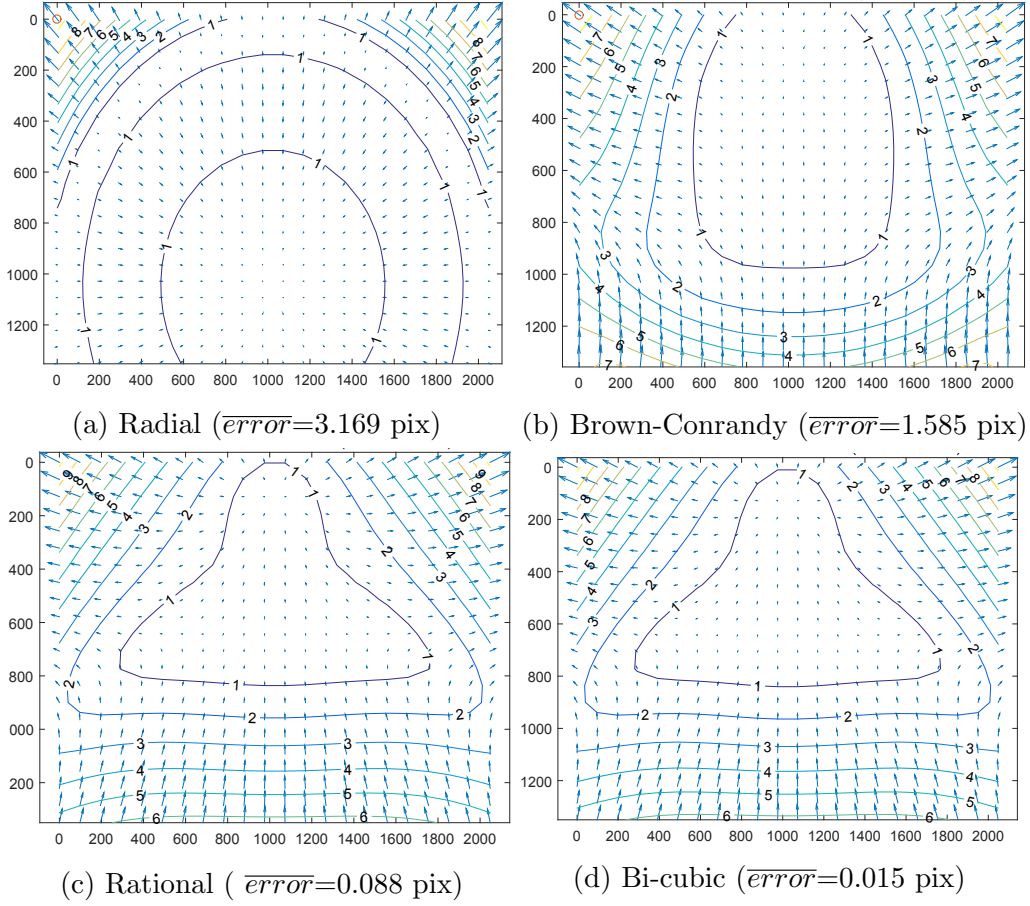


Figure 3: Models fitting results for simulated CaSSIS data. Here, and later in this paper, vectors in distortion fields graphs show how we should move points of the distorted image to get undistorted image. Contour lines show the magnitude of this motion. Errors show difference distortion predicted by the model and real distortion.

3. On-ground Calibration

After the CaSSIS camera became available, we performed on-ground calibration of the Rational lens distortion model. Calibration of other components of the geometric camera model was performed by our colleges from University of Bern. On-ground calibration procedure had two goals:

1. Confirm magnitude of the lens distortion, predicted by the simulation.
2. Estimate parameters of the Rational distortion model using real data.

In this chapter in section 1 we show calibration method, that we used to perform on-ground calibration, in section 2 we describe the calibration procedure and in section 3 we show our results.

3.1. Method

Method for calibrating the Rational lens distortion model using single chart image was developed in [4]. For calibration, we need to capture image of a regular grid pattern. Every vertex of the grid pattern $\mathbf{n} = (n, m)$ is projected by unknown camera homography \mathbf{H} to the point $\mathbf{x} = (x, y)$ in distortion-free image. The ideal image coordinates, are connected with the distorted image coordinates $\mathbf{i} = (i, j)$ via the Rational function (Equation 13), described by matrix \mathbf{A} . In homogeneous coordinates we have following equation

$$\mathbf{H}\mathbf{n} \propto \mathbf{A}\chi, \quad (16)$$

The homography matrix \mathbf{H} can be absorbed by rational distortion matrix \mathbf{A} . If we denote $\mathbf{A}_{\mathbf{H}} = \mathbf{H}^{-1}\mathbf{A}$, we can rewrite the above equation as

$$\mathbf{n} \propto \mathbf{A}_{\mathbf{H}}\chi, \quad (17)$$

This equation states that the vector on it's left side is parallel to the vector on it's right side. Since cross product of two parallel vectors is equal to zero, we can rewrite the equation as

$$[\mathbf{n}]_{\times} \mathbf{A}_{\mathbf{H}}\chi = 0, \quad (18)$$

where $[\mathbf{n}]_{\times}$ is a matrix form of a cross product [1, p581].

Using this equation, we can find the rational distortion matrix \mathbf{A} up to unknown homography. Essentially, it means that we can find matrix $\mathbf{A}_{\mathbf{H}}$ that transforms a distorted image to a distortion-free image, but on

85 the top of it, applies some unknown homography \mathbf{H}^{-1} . After applying the
86 distortion correction, described by matrix $\mathbf{A}_{\mathbf{H}}$, we get an image taken by new
87 distortion-free "virtual camera". Parameters of this "virtual camera" should
88 be estimated using the standard procedure.

89 During our experiments, we found that calibration using chart image,
90 described above, can't be used with our chart image, since it contains too
91 many outliers. To get rid of the outliers, we combined the original method
92 with inlier detection algorithm - RANSAC[1, p117]. In the RANSAC, we
93 used SVD method[1, p592] to solve the homogeneous linear least squares
94 problem. We found that it is necessary to perform z-score normalization
95 of 2D grid coordinates and "lifted" 6D distorted image coordinates, before
96 using the SVD method. In homogeneous coordinates the normalization can
97 be performed as follows

$$\begin{aligned}\mathbf{n}' &= \mathbf{T}_n \mathbf{n} \\ \chi' &= \mathbf{T}_\chi \chi\end{aligned}\tag{19}$$

After computing the solution, we perform de-normalization of the rational distortion matrix, as

$$\hat{\mathbf{A}} = \mathbf{T}_n^{-1} \hat{\mathbf{A}}' \mathbf{T}_\chi^{-1}\tag{20}$$

To detect outliers in the RANSAC, we use Sampson error[1, p99]. We refine original RANSAC solution, using Levenberg-Marquardt algorithm[1, p600] using only inliers, detected by the RANSAC. In general case, all elements of estimated matrix $\hat{\mathbf{A}}$ take different non-zero values. However, in [4] authors suggest to use following "canonical" form of the matrix:

$$\mathbf{A} = \begin{bmatrix} \times & \times & \times & \times & 0 & 0 \\ \times & \times & \times & 0 & \times & 0 \\ \times & \times & \times & \times & \times & \times \end{bmatrix}.\tag{21}$$

98 Any "non-canonical" matrix $\hat{\mathbf{A}}$ can multiplied by specially designed ho-
99 mography matrix and "canonicalized". There is an infinite number of possi-
100 ble "canonicalizing" homographies. In order to minimize image distortions,
101 we simply assume that the desired homography is affine and all its diago-
102 nal elements are equal to one. This assumption allows us to select single
103 "canonicalizing" homography from the infinite set.

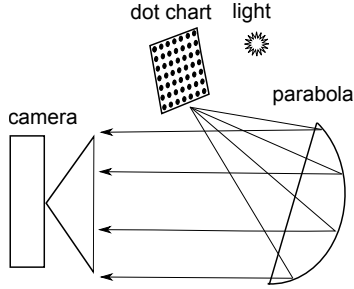


Figure 4: On-ground calibration settings.

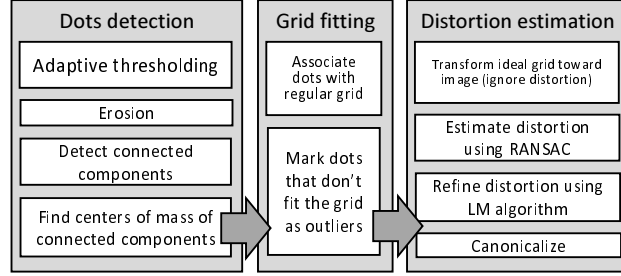


Figure 5: On-ground lens distortion calibration procedure.

104 3.2. Procedure

105 Since focal length of the CaSSIS camera is too large to directly capture
 106 in-focus image from reasonably close distance, we use experimental setting
 107 shown in Figure 4 (the chart is placed in focus of the parabolic collimator).
 108 These settings are not ideal, since distortion, caused by the collimator itself
 109 is added to the CaSSIS lens distortion. However, we assume that distortion
 110 of the collimator are significantly smaller than distortion of the CaSSIS lens.

111 To calibrate the Rational lens distortion model, we follow the procedure
 112 shown in Figure 5. Firstly, we detect dots in the chart image. To find the
 113 dots' centers with sub-pixel accuracy, we use weighted center-of-mass algo-
 114 rithm. Next, we fit the grid to the dots, detected in the image. To fit the
 115 grid to the dots, we use simple greedy algorithm that starts from arbitrary
 116 selected dot and expands the grid in horizontal and vertical directions, until
 117 no new dots can be added to the grid. We run the algorithm several times,
 118 and select grid fitting result with largest number of fitted dots. Then, we
 119 estimate a homography transformation that brings the ideal grid closer to
 120 its image. We apply this transform to the ideal grid and continue calibra-
 121 tion with this transformed grid. In this way, we "minimize" homography
 122 transform that gets absorbed into the estimated rational distortion matrix.
 123 Finally, we run the distortion estimation algorithm, described earlier.

124 3.3. Results

125 As shown in Figure 6, our dots detection and grid fitting algorithm was
 126 able to find almost all dots of the grid pattern, despite of low image contrast

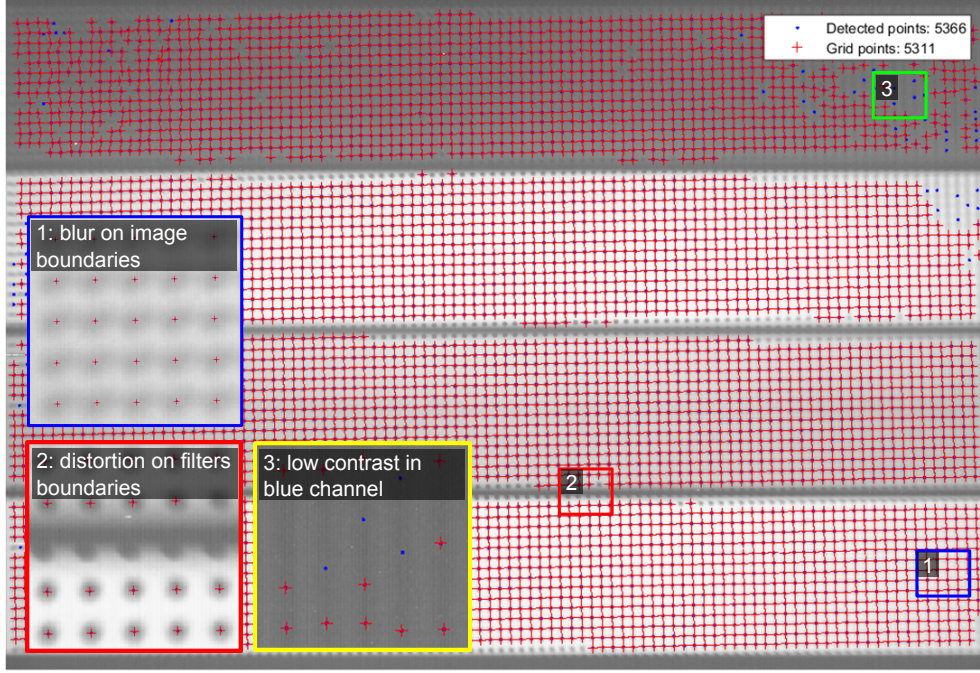


Figure 6: Dots detection and grid fitting result.

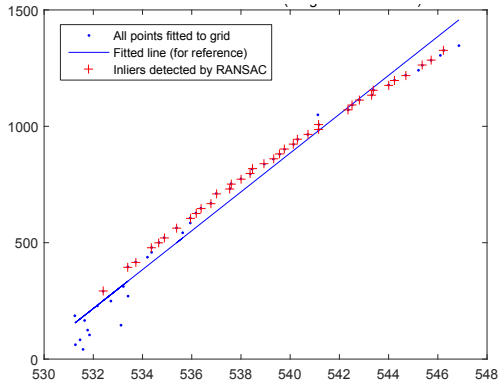


Figure 7: Image coordinates of dots, that belong to single row of the grid pattern.

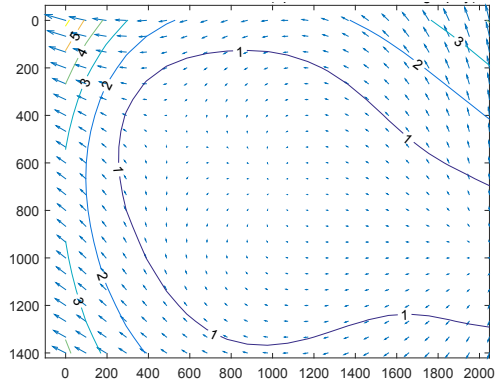


Figure 8: Experimental distortion field of CaSSIS lens.

127 in the blue filter, significant blur on the image boundaries⁵ and distortions
 128 on the boundaries between the filters. By looking at the image of dots that
 129 belong to single grid row (Figure 7), we confirmed presence of small lens
 130 distortion in the image: the grid row appeared not as a straight line, but
 131 as a high-order curve. We also observed, that our algorithm detected useful
 132 point together with outliers. Subsequent RANSAC algorithm successfully
 133 eliminated most of the outliers. As we expected, most of the outliers were
 134 detected on the boundaries of the image, in the blue filter and between the
 135 filters. After refinement of the initial solution using Levenberg-Marquardt al-
 136 gorithm and "canonicalization" of the solution, we got distortion field shown
 137 in Figure 8. It looks different from the distortion field predicted by sim-
 138 ulation, but this is possible for two reasons. Firstly, we don't know what
 139 distortion is introduced by the parabolic collimator. Secondly, we can find
 140 the distortion field only up to unknown homography. To confirm validity of
 141 estimated Rational model, we undistorted another dot chart image, acquired
 142 by the CASSIS, using the estimated Rational model. We compared distri-
 143 butions of Euclidean distances from dots to grid lines⁶ before and after the
 144 distortion correction. As shown in Figure 10, the median distance decreased
 145 more than twice after the distortion correction. Examination of the dots that
 146 belong to the same grid row also showed that grid lines were straightened by
 147 the distortion correction procedure (Figure 9).

148 To summarize, during the on-ground calibration:

- 149 1. We confirmed presence of lens distortion in CaSSIS image. The max-
 150 imum distortion magnitude is about 5 pixel on the boundaries of the
 151 image.
- 152 2. We estimate parameters of Rational lens distortion model using the
 153 real data and showed that using our model we can correct the image
 154 and decrease image's non linearities more than twice.

155 4. In-flight Calibration

156 After launch of the orbiter, we will perform in-flight calibration of the
 157 geometric camera model. This procedure is important, since the camera pa-

⁵The parabolic collimator can bring in perfect focus of the CaSSIS lens only dots that are placed in its focus, all other dots inevitable have some out-of-focus blur.

⁶Lines were fitted to dots that belong to same grid row/column using linear regression.

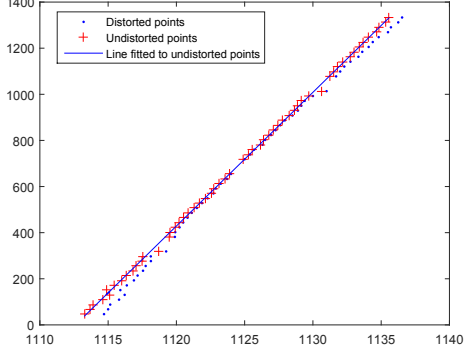


Figure 9: Image coordinates of the dots, that belong to single row of the pattern grid, before and after distortion correction.

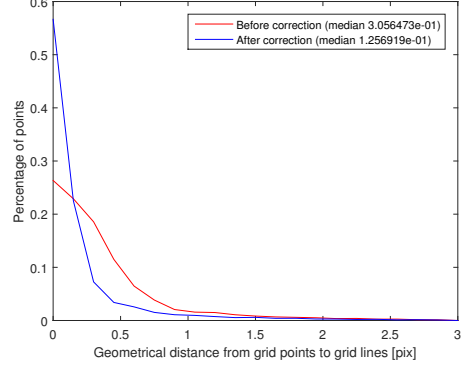


Figure 10: Distribution of Euclidean distances between image of grid dots and straight lines before and after distortion correction.

rameters can change during the launch of the spacecraft. In this chapter, in section 1 we describe method, that we use for in-flight calibration of intrinsic, extrinsic and lens distortion models. In section 2, we show the in-flight calibration procedure and in section 3 we present results of in-flight calibration simulation.

4.1. Method

The positions of many stars are well documented in star catalogs, therefore we can use stars as a calibration targets. Stars positions are typically given in spherical Equatorial coordinate frame and are fixed in time⁷. Spherical coordinates can be easily converted to rectangular Equatorial coordinates as follows

$$\mathbf{X} = \begin{bmatrix} X \\ Y \\ Z \end{bmatrix} = \begin{bmatrix} r \cos \alpha \cos \delta \\ r \sin \alpha \cos \delta \\ r \sin \delta \end{bmatrix}, \quad (22)$$

where r is a distance to the star, α is a right ascension angle and δ is a declination angle.

⁷In reality, stars slowly move due to "proper motion" phenomenon, but this motion is negligibly slow.

171 Lets assume that we know correspondences between 3D position of star in
 172 rectangular Equatorial coordinate frame $\mathbf{X} = (X, Y, Z)$ and it's 2D position
 173 in the distorted image $\mathbf{i} = (i, j)$. In this case, in homogeneous coordinates
 174 we can write

$$\mathbf{A}\chi \propto \mathbf{P}\mathbf{X}, \quad (23)$$

175 where \mathbf{A} is 6×3 rational distortion matrix, \mathbf{P} is 3×4 camera projection
 176 matrix and $\chi = [i^2 \ ij \ j^2 \ i \ j \ 1]^T$ is 6×1 vector of "lifted" to 6D coordinates of
 177 star in the distorted image. The camera projection matrix can be factorized
 178 as following

$$\mathbf{P} \propto \mathbf{K}[\mathbf{R}|\mathbf{t}], \quad (24)$$

179 where \mathbf{K} is 3×3 camera intrinsic matrix, \mathbf{R} and \mathbf{t} are 3×3 rotation matrix and
 180 3×1 translation vector of the camera with respect to rectangular Equatorial
 181 coordinate frame. Since the distance from the spacecraft to origin of the
 182 Equatorial coordinate system is negligible compare to distance to the stars,
 183 we can ignore translation of the camera frame and rewrite Equation 24 as
 184 follows

$$\mathbf{P} \propto \mathbf{K}\mathbf{R}, \quad (25)$$

185 The rotation matrix \mathbf{R} is approximately know, since we know the orienta-
 186 tion of the spacecraft with respect to the rectangular Equatorial coordinate
 187 system⁸ and the orientation of camera with respect to the spacecraft. How-
 188 ever, we assume that there is a small systematic error $(\Delta\alpha, \Delta\beta, \Delta\gamma)$ in the
 189 orientation, due to the camera mounting error, and parametrize rotation
 190 matrix as following

$$\mathbf{R} = \mathbf{R}_{\alpha+\Delta\alpha} \cdot \mathbf{R}_{\beta+\Delta\beta} \cdot \mathbf{R}_{\gamma+\Delta\gamma} \quad (26)$$

191 Now lets rewrite Equation 23, substituting for camera projection matrix
 192 from Equation 25, as follows

$$\mathbf{A}\chi \propto \mathbf{K}\mathbf{R}\mathbf{X}, \quad (27)$$

⁸The rotation of the spacecraft with respect to the Equatorial frame is constantly monitored by attitude control system.

Looking at the Equation 23, we can notice that simultaneous presence of intrinsic matrix \mathbf{K} and full rational distortion matrix \mathbf{A} and rotation matrix \mathbf{R} creates parameters redundancy (or coupling)⁹:

1. Matrices \mathbf{K} and \mathbf{A} can both shift image coordinates.
2. Matrices \mathbf{R} and \mathbf{A} can both rotate image coordinates.
3. Matrices \mathbf{K} and \mathbf{A} can both scale images coordinate.

Therefore, with the full rational distortion matrix \mathbf{A} we are not able to determine focal lengths α_x, α_y , principal points x_0, y_0 and rotations $(\Delta\alpha, \Delta\beta, \Delta\gamma)$ uniquely. Clearly, we need to modify rational distortion matrix to get rid of the parameterization redundancies (coupling).

Lets firstly assume that there is a point in the center of the image - center of distortion, that does not undergo the distortion. In other words, lets assume that in the center of the image matrix \mathbf{A} effectively disappears. For convenience, lets set origin of the distorted image coordinate system in this point. Next, lets linearize vector distortion function $\mathbf{x} = \mathbf{F}(\mathbf{i})$ (Equation 13) around this point as follows

$$\mathbf{F}(\mathbf{i}) = \mathbf{F}(\mathbf{0}) + \mathbf{dF}/\mathbf{di}|_{\mathbf{i}=\mathbf{0}} \quad (28)$$

where $\mathbf{dF}/\mathbf{di}|_{\mathbf{i}=\mathbf{0}}$ is a Jacobian of function $\mathbf{F}(\mathbf{i})$ at $\mathbf{i} = \mathbf{0}$ equal to

$$\mathbf{dF}/\mathbf{di}|_{\mathbf{i}=\mathbf{0}} = \begin{bmatrix} a_{14}/a_{36} - a_{16}a_{34}/a_{36}^2 & a_{15}/a_{36} - a_{16}a_{35}/a_{36}^2 \\ a_{24}/a_{36} - a_{26}a_{34}/a_{36}^2 & a_{25}/a_{36} - a_{26}a_{35}/a_{36}^2 \end{bmatrix}, \quad (29)$$

Since we assume that the neighborhood of the point $\mathbf{i} = \mathbf{0}$ does not undergo distortions, we can equate $\mathbf{F}(\mathbf{i}) = \mathbf{i}$. Clearly, this equality will be satisfied, if we set $a_{16} = a_{26} = a_{15} = a_{24} = 0$ and $a_{36} = a_{14} = a_{25} = 1$. Lets define decoupled rational lens distortion matrix as follows

$$\mathbf{A}' = \begin{bmatrix} a_{11} & a_{12} & a_{13} & 1 & 0 & 0 \\ a_{21} & a_{22} & a_{23} & 0 & 1 & 0 \\ a_{31} & a_{32} & a_{33} & a_{34} & a_{35} & 1 \end{bmatrix}, \quad (30)$$

⁹For example, if we multiply first row of the intrinsic matrix \mathbf{K} by some scalar s and, simultaneously, divide first row of the rational distortion matrix \mathbf{A} by the same scalar, nothing will change.

Obviously, the parameters of the matrix \mathbf{A}' and the parameters of the matrices \mathbf{K} and \mathbf{R} are decoupled in linear sense near center of distortion, since linear approximation of matrix \mathbf{A}' does not perform scaling, rotation and translation at this point. However, it is also obvious that matrix \mathbf{A}' has less degrees-of-freedom than the full matrix \mathbf{A} (11 out of 18 DOF). Nevertheless, we can show that the matrix \mathbf{A} combined with the matrix \mathbf{K} still allow to model wide variety of lens distortions. This is because the translation and scaling can be effectively "reintroduced" into the matrix \mathbf{A}' from the matrix \mathbf{K} . Therefore, the matrix \mathbf{A}' , when used with the matrix \mathbf{K} , has same descriptive power as matrix

$$\mathbf{A}'' = \begin{bmatrix} a_{11} & a_{12} & a_{13} & a_{14} & a_{16} * a_{35} & a_{16} \\ a_{21} & a_{22} & a_{23} & a_{26} * a_{34} & a_{25} & a_{26} \\ a_{31} & a_{32} & a_{33} & a_{34} & a_{35} & 1 \end{bmatrix}, \quad (31)$$

In the following experimental section, we show that this matrix is powerful enough to represent even complex lens distortion of CaSSIS lens.

Now, when we decoupled intrinsic, extrinsic and lens distortion parameters, lets return to the Equation 27. This equation states that the vector on it's left side is parallel to the vector on it's right side. Since cross product of two parallel vectors is equal to zero, we can rewrite Equation 27 as

$$[\mathbf{A}'\chi]_{\times} \mathbf{K} \mathbf{R} \mathbf{X} = \mathbf{0}, \quad (32)$$

The Equation 32 is written only for one star in one image. Now lets assume that we have $n = 1 \dots N$ images with $m = 1 \dots M_n$ stars in every image. In this case, we can write equations similar to Equation 32 for every star in every image as follows

$$\left\{ \begin{array}{l} [\mathbf{A}'\chi_{11}]_{\times} \mathbf{K} \mathbf{R}_1 \mathbf{X}_{11} = \mathbf{0} \\ \dots \\ [\mathbf{A}'\chi_{1M_1}]_{\times} \mathbf{K} \mathbf{R}_1 \mathbf{X}_{1M_1} = \mathbf{0} \\ \dots \\ [\mathbf{A}'\chi_{N1}]_{\times} \mathbf{K} \mathbf{R}_N \mathbf{X}_{N1} = \mathbf{0} \\ \dots \\ [\mathbf{A}'\chi_{NM_N}]_{\times} \mathbf{K} \mathbf{R}_N \mathbf{X}_{NM_N} = \mathbf{0} \end{array} \right., \quad (33)$$

Every every sub-system in this system corresponds to one image and every vector equation corresponds to one star. For every star, we can write 3 scalar

232 equations. In this system we have 18 DOF in total:

- 233 1. 3 DOF for extrinsic parameters: systematic rotation errors $\Delta\alpha$, $\Delta\beta$
234 and $\Delta\gamma$.
- 235 2. 4 DOF for intrinsic parameters: focal lengths α_x , α_y and principal
236 points x_0 and y_0 .
- 237 3. 11 DOF for lens distortion parameters: a_{11} , a_{12} , a_{13} , a_{21} , a_{22} , a_{23} , a_{31} ,
238 a_{32} , a_{33} , a_{34} and a_{35} .

239 This system of equations can be initialized by nominal values of intrinsics,
240 zero rotation errors and zero distortion coefficients. It can be, then, solved
241 using Levenberg-Marquardt iterations. However, firstly we equalize scale of
242 all parameters, otherwise the convergence of the method will be slow. This
243 can be achieved by normalizing distorted and undistorted image coordinates
244 to the range $[-1, 1]$. In homogeneous coordinates the normalization can be
245 performed as follows

$$\begin{aligned}\mathbf{x}' &= \mathbf{T}_x \mathbf{x} \\ \mathbf{i}' &= \mathbf{T}_i \mathbf{i}\end{aligned}\tag{34}$$

246 In this way, large elements of matrix \mathbf{K} , that correspond to the focal
247 lengths, will be significantly reduced. Of course, if we use coordinates scaling,
248 after solving the Equation 33 we have to de-normalize the matrix $\hat{\mathbf{K}}$ as follows

$$\hat{\mathbf{K}} = \mathbf{T}_x^{-1} \hat{\mathbf{K}}' \tag{35}$$

249 4.2. Procedure

250 We don't yet have in-flight data for our CaSSIS camera. Therefore, for
251 simulation of the in-flight calibration procedure we use freely available data
252 from CASSINI mission, including images¹⁰ and SPICE kernels¹¹. As a source
253 of information about stars, we use Tycho2 star catalog¹², that contains infor-
254 mation about approximately 2.5 million stars. The overall work flow of the

¹⁰Images are available on Planetary Image Atlas website <http://pds-imaging.jpl.nasa.gov/search/>

¹¹SPICE kernels include all information about orientation and position of spacecraft of any NASA mission at any moment in time. They are available on PDS SPICE Archive website http://naif.jpl.nasa.gov/naif/data_archived.html

¹²Catalog is freely available on Vizier website <http://vizier.u-strasbg.fr/cgi-bin/VizieR?-source=Tycho-2>

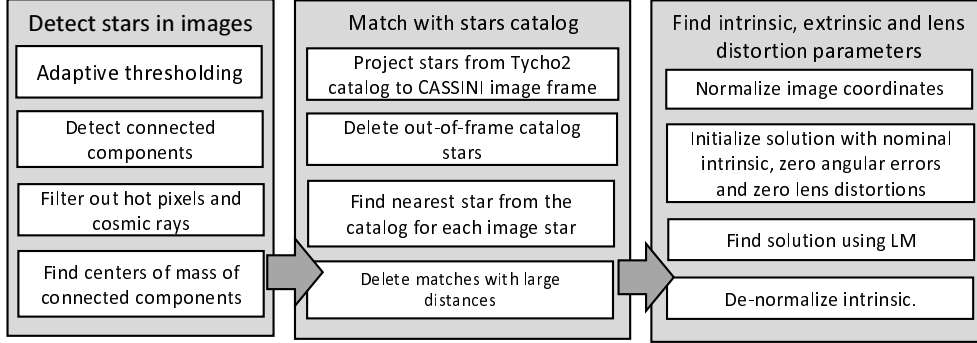


Figure 11: In-flight calibration procedure work flow.

in-flight calibration procedure is shown in Figure 11. Firstly, we binarize the image using procedure described in [7, p.39]. When we perform connected components analysis on binary image, and discard line-like and small connected components, since they are most probably correspond to cosmic rays and hot pixels. Next, we find centers of mass of the remaining connected components with sub pixel precision.

Next, we associate every star-like object from the image with the star from the Tycho2 catalog. For that, we firstly re-project all stars from the Tycho2 catalog onto CASSINI image frame. To do this, we use spacecraft orientation parameters, given at the image acquisition time, and approximate intrinsic parameters from the SPICE kernel. We discard all stars, that project outside of the image frame. After that, we associate every star-like object in the image with the nearest star from the catalog, provided that they are sufficiently close in the image. We found that this simple procedure works well, if the original extrinsic and intrinsic estimates are good enough.

After that, we construct the Equation 33 and solve it as described in previous section.

4.3. Results

Firstly, we checked if rational distortion function with decoupled matrix \mathbf{A}'' (Equation 31) is powerful enough to represent CaSSIS lens distortion, given by Table 1. To do this, we fitted the model with decoupled matrix to the data and checked the errors. The result of this experiment is shown in Figure 15. Concluding from the figure, the decoupled matrix gives almost identical results to full distortion matrix, and thus can be used in the in-flight calibration.

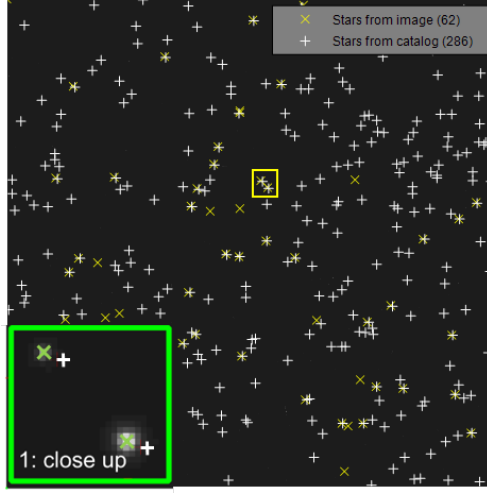


Figure 12: Result of stars detection and catalog stars re-projection.

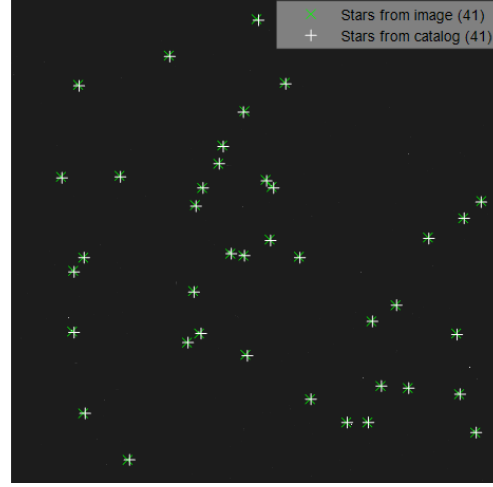


Figure 13: Result of stars matching (same star field as in Figure 12).

280 Next, we checked performance of our star detection and matching proce-
 281 dure using CASSINI images. We processed 37 CASSINI images and found
 282 that in most of images we were able to recognize 10-20 stars. We also found
 283 that the extrinsic/intrinsic parameters in SPICE kernels are precise and Eu-
 284 clidean distances between catalog star projections and image stars are typ-
 285 ically less than 10 pixels. Result of the stars detection and catalog stars
 286 re-projection is shown in Figure 12, and result of stars matching is shown in
 287 Figure 13.

288 To prove that at least some matches in Figure 13 are not accidental, we
 289 performed Monte-Carlo simulation. In this simulation we sampled 62 image
 290 stars positions and 268 catalog star positions from uniform distribution and
 291 counted number of matches. After 100 repetitions of the simulation, we got
 292 distribution of number of random matches, show in Figure 14. As we can
 293 see, the average number of the random matches is equal to 2, whereas in our
 294 case we got 41 matches. It is obvious, that most of these matches represent
 295 actual relationships between the catalog and the image stars. However, it is
 296 also obvious, that some of these matches are outliers.

297 Next, we checked effectiveness of our calibration routine. We ran our
 298 calibration procedure on 20 training images and obtained new parameters,
 299 shown in Table 3. The distortion field, shown in Figure 16, is consistent with
 300 the distortion reported in [8] (Figure 17).

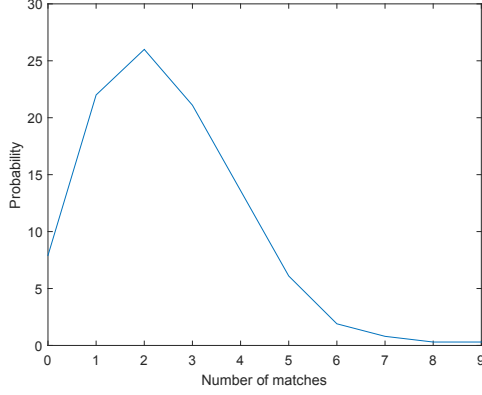


Figure 14: Probability distribution for number of random matches (same star field as in Figure 12).

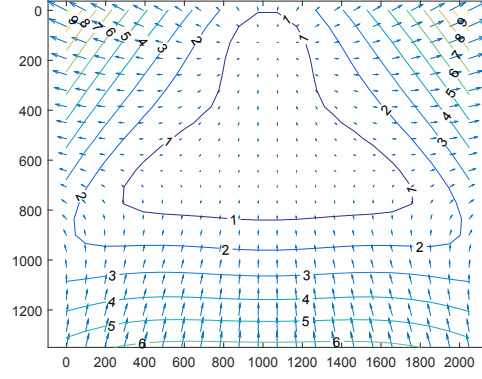


Figure 15: Distortion field of Rational distortion model with decoupled matrix fitted to data from Table 1: $\overline{error}=0.09$.

Parameters	Old values	New values
Extrinsic: ($\Delta\alpha, \Delta\beta, \Delta\gamma$, [deg])	(0, 0, 0)	($1.8 \cdot 10^{-3}, 3.2 \cdot 10^{-3}, 6.2 \cdot 10^{-3}$)
Intrinsic: (α_x, α_y), [pix] (x_0, y_0), [pix]	(16731, 16731) (512, 512)	(16726, 16731) (511, 513)
Lens distortion: $\begin{bmatrix} a_{11} & a_{12} & a_{13} & 1 & 0 & 0 \\ a_{21} & a_{22} & a_{23} & 0 & 1 & 0 \\ a_{31} & a_{32} & a_{33} & a_{34} & a_{35} & 1 \end{bmatrix}$	$\begin{bmatrix} 0 & 0 & 0 & 1 & 0 & 0 \\ 0 & 0 & 0 & 0 & 1 & 0 \\ 0 & 0 & 0 & 0 & 0 & 1 \end{bmatrix}$	$\begin{bmatrix} 0.4 & -0.22 & 0 & 1 & 0 & 0 \\ 0 & 0.4 & -0.21 & 0 & 1 & 0 \\ 0.03 & 0 & 0.04 & 0.4 & -0.22 & 1 \end{bmatrix}$

Table 3: Extrinsic, intrinsic and lens distortion parameters before and after in-flight calibration (new lens distortion parameters are visualized in Figure 16).

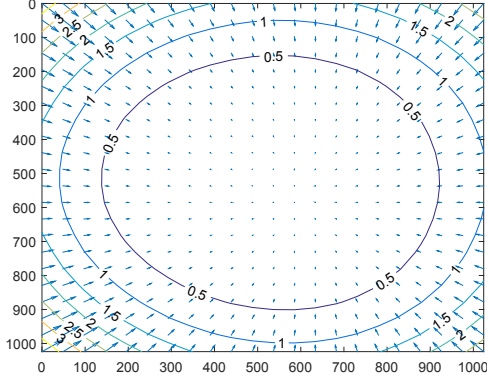


Figure 16: Lens distortion field after in-flight calibration. Distortion parameters' values are shown in Table 3.

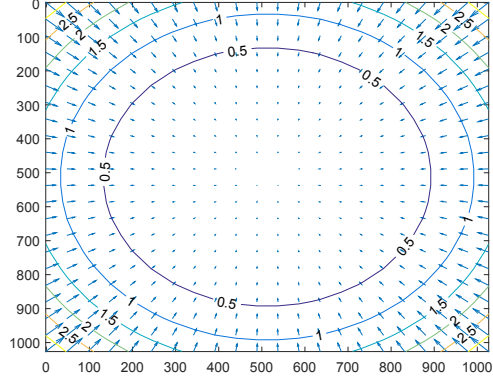


Figure 17: CASSINI WAC lens distortion field reported in [8].

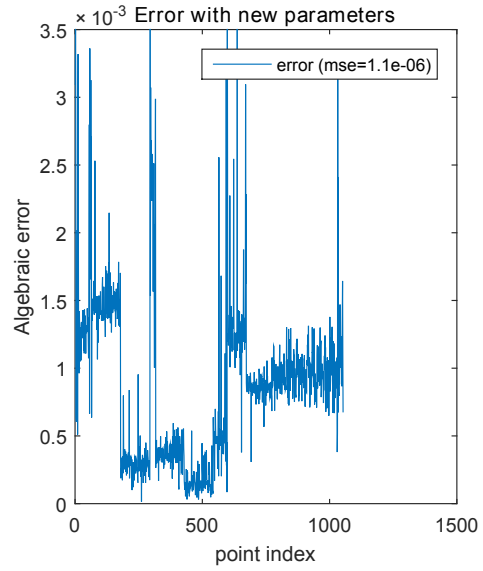
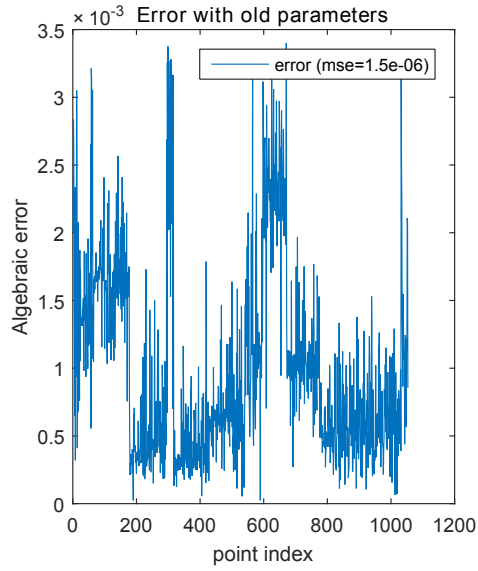


Figure 18: In-flight calibration test set errors (20 images used for training and another 17 images are used for testing).

301 Then, we checked calibration error using test set. In Figure 18 we show
 302 algebraic error for test set for the original parameters and the optimized
 303 parameters. Observing the figure, we noticed that the calibration procedure
 304 minimizes the errors, on average, however it increases the error in the certain
 305 points. We think these points might be an outliers. We also noticed that
 306 there is a bias in the error, that is different for different images. This is
 307 probably because, besides the systematic error, there is a random error in
 308 the orientation estimates, provided by the attitude control system. These
 309 random errors can not be corrected by our calibration routine.

310 Next, we checked how parameters estimates converge as number of train-
 311 ing images increases. For that, we performed parameters estimation with
 312 different number of training images ranging from 1 to 37. Results of the
 313 experiment is shown in Figure 19, Figure 20, Figure 21 and Figure 22. Ob-
 314 serving the figures, we concluded that as number of training images grows,
 315 our parameter estimates become more stable. However, different parameters
 316 converge to the stable values with the different speed. For example, lens
 317 distortion parameters converge very slowly, probably because their relative
 318 effect on the image is subtle. Concluding from the figure, 20-25 images of
 319 stars with 10-20 stars in each image should be enough to calibrate the model.

320 Summarizing the in-flight calibration simulation result:

- 321 1. We developed the procedure for automatic matching of stars from the
 322 image with stars from the catalog. With CASSINI we get approxi-
 323 mately 10-20 matches per star image (with 1-2 outliers).
- 324 2. We developed the procedure for calibration of intrinsic, extrinsic and
 325 lens distortion parameters using identified stars from several images.
 326 We showed that 20-25 images with 10-20 stars in each image is enough
 327 for calibration.
- 328 3. We proposed a method that allows to calibrate rational distortion
 329 model using star images. This result is significant since rational lens
 330 distortion model is universal model that can be used with wide variety
 331 of lenses.

332 [1] R. Hartley, A. Zisserman, Multiple View Geometry in Computer Vision,
 333 Cambridge University Press, 2003.

334 [2] J. G. Fryer, D. C. Brown, Lens distortion for close-range photogrammetry,
 335 Photogrammetric engineering and remote sensing (1986) 51–58.

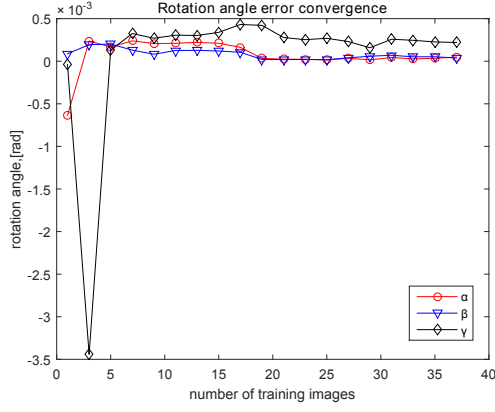


Figure 19: Estimates of systematic rotation angle errors versus number of training images.

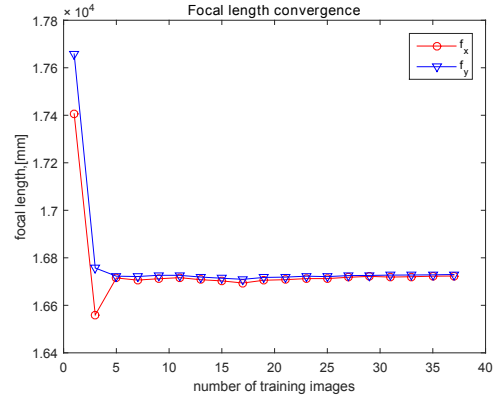


Figure 20: Estimates of focal lengths versus number of training images.

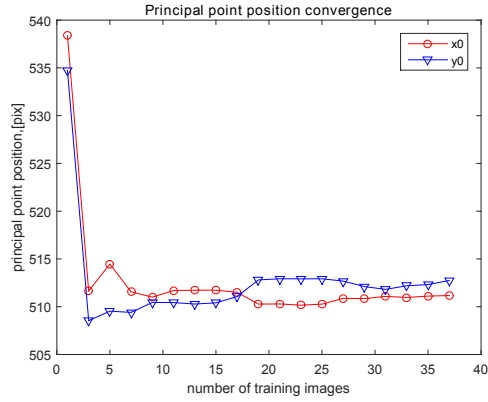


Figure 21: Estimates of principal points versus number of training images.

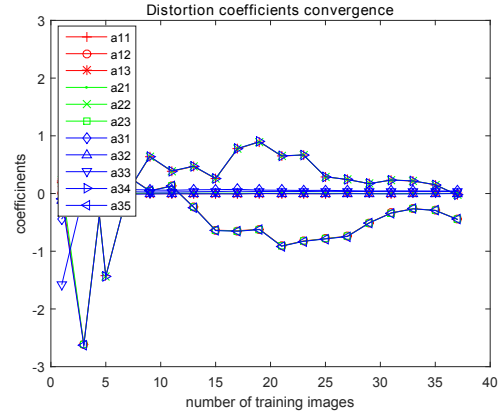


Figure 22: Estimates of distortion coefficients versus number of training images.

- 336 [3] E. Kilpel, Compensation of systematic errors of image and model coor-
 337 dinates, *Photogrammetria* 37 (1981) 15–44.
- 338 [4] D. Claus, a.W. Fitzgibbon, A rational function lens distortion model for
 339 general cameras, 2005 IEEE Computer Society Conference on Computer
 340 Vision and Pattern Recognition (CVPR’05) 1 (2005).
- 341 [5] K. Di, R. Li, CAHVOR camera model and its photogrammetric conver-
 342 sion for planetary applications, *J. Geophys. Res.* 109 (2004) E04004.
- 343 [6] Z. Tang, R. V. Gioi, P. Monasse, J. Morel, Self-consistency and univer-
 344 sality of camera lens distortion models (2012) 1–22.
- 345 [7] D. Lang, Astrometry.net: Blind astrometric calibration of arbitrary as-
 346 tronomical images, Ph.D. thesis, 2010.
- 347 [8] Cassini imaging science: Instrument characteristics and anticipated scien-
 348 tific investigations at Saturn, *Space Science Reviews* 115 (2005) 363–497.